

Ceramic nuclear fuel fracture modeling with the extended finite element method

Wen Jiang^a, Benjamin W. Spencer^a, John E. Dolbow^b

^a Idaho National Laboratory, Idaho Falls, ID 83415-3840, United States

^b Civil and Environmental Engineering, Duke University, Durham, NC 27708-0287, United States

ARTICLE INFO

Keywords:

Extended finite element method
Thermal-mechanics
Fuel fracture

ABSTRACT

Ceramic fuel pellets used in nuclear light water reactors experience significant fracture due to the high thermal gradients experienced under normal operating conditions. This has important effects on the performance of the fuel system. Because of this, a realistic, physically based fracture modeling capability is essential to predict fuel behavior in a wide variety of normal and off-normal conditions. The extended finite element method (X-FEM) is a powerful method to represent arbitrary propagating discrete cracks in finite element models, and has many characteristics that make it attractive for nuclear fuel performance analysis. This paper describes the implementation of X-FEM in a multiphysics fuel performance code and presents applications of that capability. These applications include several thermal mechanics fracture benchmark problems, which demonstrate the accuracy of this approach. It also includes application of this capability to study nuclear fuel fracture, both on stationary and propagating cracks. The study on stationary cracks shows the effects of interactions between cracks, and aids in understanding the process of crack propagation during a power ramp. The propagating crack case demonstrates random initiation and subsequent propagation of interacting thermally induced cracks during an initial ramp to full power with fresh fuel.

1. Introduction

Nuclear light water reactors (LWRs) use a fuel system that consists of long hollow metal (typically zirconium alloy) rods that contain hundreds of stacked cylindrical ceramic uranium oxide fuel pellets. During normal operation, nuclear fission volumetrically heats the fuel pellets, and this heat is transferred to water coolant circulating axially along the fuel rods. This volumetric heating within the fuel and cooling on the outer surface of the fuel generates a strong thermal gradient in the radial direction in the fuel. Non-uniform volumetric expansion due to these thermal gradients as well as other effects causes tensile stresses high enough to result in fracture. Fracture occurs very early in the life of the fuel, starting early in the initial ramp to full power with fresh fuel.

Fuel fracture is not a direct safety concern, as the fuel is contained within metal rods that prevent the release of fission products to the coolant. However, fuel fracture does play an important role in the performance of the fuel system, and its effects must be accounted for to accurately predict fuel behavior. The thermal stresses under normal operating conditions cause the formation of radial and axial cracks. These cracks decrease the constraint in the regions where they form, which results in an increase in the average pellet diameter relative to an uncracked pellet. In addition, these cracks permit the occurrence of a phenomenon known as radial relocation, in which fuel fragments move radially outward from the fuel centerline. Radial relocation decreases the size of the gap between the pellet and cladding and enhances the thermal conductance across that gap, while decreasing the effective conductivity of the fuel in directions normal to cracks. Later in the life of the fuel rod, when the fuel comes in contact with the cladding due to a combination of volumetric swelling of the fuel and inward creep of the cladding, fuel cracking can also play a significant role

<https://doi.org/10.1016/j.engfracmech.2019.106713>

Received 11 June 2019; Received in revised form 3 October 2019; Accepted 5 October 2019

Available online 24 October 2019

0013-7944/ © 2019 Elsevier Ltd. All rights reserved.

in cladding failure. Stress concentrations that occur in the cladding adjacent to cracks intersecting the outer surface of the fuel can lead to cladding failure in a phenomenon known as pellet-cladding mechanical interaction (PCMI).

There have been a number of efforts to develop realistic, physically based fracture modeling capabilities for fuel performance analysis, motivated by an interest in predicting fuel behavior in a wide variety of normal and abnormal conditions. Within the context of the finite element method (FEM), the smeared cracking model [1] is widely used in current fuel performance codes [2–4]. Smeared cracking represents cracks using a softening material constitutive model that degrades the stiffness and strength at integration points. Smeared cracking is straightforward to implement and use, and has the effect of globally reducing stresses due to cracking, although it suffers from well-known mesh dependencies that tend to prevent it from correctly modeling crack localization [5]. Alternatively, fracturing nuclear fuel has been successfully modeled using cohesive zone models with interface elements to represent discrete fracture [6]. A major shortcoming of this method, however, is that crack paths must be defined prior to running a simulation. Recently, particle-based and meshfree discretization techniques, such as the discrete element method (DEM) [7] and peridynamic theory [8–11], have been used to model cracking in ceramic nuclear fuel pellets. The key advantage of those methods lies in the fact that cracks can nucleate and grow in an unguided manner. However, the computational cost of those methods can be very high and there are a number of challenges still to be addressed to use them in an engineering fuel performance code. For example, including nonlinear constitutive behavior such as creep and plasticity still remains an open research topic.

Because the standard FEM is based on assumptions of spatially continuous behavior, representing discontinuities such as those arising from cracks within that method is inherently problematic. The eXtended Finite Element Method (X-FEM) was introduced [12] as a technique that allows for arbitrary spatial discontinuities to be represented within the context of FEM. The X-FEM allows for discrete cracks to traverse a domain discretized with a finite element mesh without explicitly fitting the mesh to the crack geometry. The X-FEM accomplishes this by enriching the finite-element approximation and adding extra degrees of freedom associated with the discontinuities. The X-FEM has the strengths of the standard FEM for representing continuous behavior, while addressing its shortcomings for addressing discontinuous behavior.

Because of its strengths in modeling discrete fracture and its basis in FEM, X-FEM is a natural fit for modeling fracture in a finite-element-based nuclear fuel performance code. This paper describes the implementation of a coupled thermal-mechanical X-FEM capability in the Bison [4] fuel performance code, and demonstrates the application of that capability to both general thermal-mechanical fracture problems as well as to LWR fuel fracture. This builds on an early version of this work initially presented in [13].

This paper is organized as follows: Section 2 defines the governing equations solved in the thermo-mechanics applications considered here. Section 3 summarizes the phantom node method used to implement the X-FEM in the present work, followed by a discussion of the implementation of this algorithm in the MOOSE framework that the Bison code is based on in Section 4. Section 5 discusses the criteria used for crack initiation and propagation. Application of the multiphysics X-FEM to several numerical validation examples and LWR fuel pellet cracking problems are presented in Section 6. Finally, concluding remarks are provided in Section 7.

2. Governing equations

The focus of the present work is on using X-FEM to model discontinuities arising from stationary and propagating fractures in coupled thermo-mechanics problems. The physical behavior of these problems is governed by fully-coupled partial differential equations for energy and momentum conservation. In the continuous portion of the solution domain, the energy balance is given in terms of the heat conduction equation:

$$\rho C_p \frac{\partial T}{\partial t} + \nabla \cdot \mathbf{q} = Q, \quad (1)$$

where T , ρ , C_p and Q are the temperature, density, specific heat and heat source, respectively. The heat flux is given as

$$\mathbf{q} = -k \nabla T, \quad (2)$$

where k denotes the thermal conductivity of the material.

Momentum conservation in the continuous portion of the domain is governed by static equilibrium at each time increment using Cauchy's equation:

$$\nabla \cdot \boldsymbol{\sigma} + \rho \mathbf{f} = 0, \quad (3)$$

where $\boldsymbol{\sigma}$ is the Cauchy stress tensor and \mathbf{f} is the body force per unit mass (e.g. gravity). The constitutive behavior is elastic in the cases considered here, and is expressed as $\boldsymbol{\sigma} = \mathbf{E}(\boldsymbol{\varepsilon} - \boldsymbol{\varepsilon}_{th})$, where \mathbf{E} is the elasticity tensor, $\boldsymbol{\varepsilon}$ is the total strain, and $\boldsymbol{\varepsilon}_{th}$ is the thermally-induced strain.

In the present work, it is assumed that fracture introduces discontinuities in both the temperature and displacement fields. For simplicity, it is assumed that there is no heat flux across the fracture, and that the fracture surfaces are traction-free. This zero-flux interface behavior is obtained if no special treatment is applied to the physics models at the X-FEM interfaces. Flux boundary conditions can in general be applied across these X-FEM interfaces to represent heat transfer in the thermal system or behavior such as decohesion and contact in the mechanical system, but that is outside the scope of the work described here.

3. Phantom-node-based X-FEM

The X-FEM approach as originally proposed [14,12] enriches the standard continuous finite element interpolation of the solution

field \mathbf{u} as a function of spatial coordinate \mathbf{x} and time t with Heaviside and near-tip enrichment functions:

$$\mathbf{u}(\mathbf{x}, t) = \underbrace{\sum_{I=1}^n N_I(\mathbf{x}) \mathbf{u}_I(t)}_{\text{Continuous}} + \underbrace{\sum_{J=1}^n N_J(\mathbf{x}) H(\mathbf{x}) \mathbf{b}_J(t)}_{\text{Heaviside Enriched}} + \underbrace{\sum_{K=1}^n N_K(\mathbf{x}) \sum_{L=1}^4 F_L(\mathbf{x}) \mathbf{c}_K^L(t)}_{\text{Near-tip Enriched}} \quad (4)$$

where n is the number of nodes per finite element, N_I are the standard finite element interpolation functions, \mathbf{u}_I are the nodal displacements, H is the Heaviside function, \mathbf{b}_J are additional nodal degrees of freedom corresponding to Heaviside enrichment, F_L are a set of enrichment functions that capture asymptotic near-tip fields, and \mathbf{c}_K are additional nodal degrees of freedom corresponding to the near-tip enrichment. This approach requires an additional degree of freedom per solution variable for each node whose support is traversed by a crack for Heaviside enrichment, as well as 4 additional degrees of freedom per solution variable for the nodes in the vicinity of the crack tip to which near-tip enrichment is applied. The set of enriched nodes is typically a small subset of the nodes in the discretized solution because a small fraction of the solution domain is typically directly affected by cracking. As a result, this does not drastically increase the number of unknowns in the system of equations. However, this can be difficult to implement in existing FEM codes if they do not permit nodes to have arbitrary number of degrees of freedom.

The phantom node method [15] was also proposed as a technique for modeling mesh-independent fracture. In the phantom node method, elements intersected by a crack are deleted and replaced by two elements that occupy the same physical locations as the original elements. A portion of the domain of each of these new elements (partial elements) represents physical material. The combined physical portions of the partial elements cover the entire domain of the original element that was split. The nodes connected to the non-physical portions of those elements are known as phantom nodes. The solution field is interpolated on the partial elements using the standard finite element shape functions. When fields are integrated on partial elements, as is done to compute an element's contribution to the residual, the integral is only performed over the physical part of the element. Shortly after the phantom node technique was proposed, it was shown [16] to give exactly the same enrichment as the originally proposed X-FEM (without the near-tip enrichment functions), and add the same number of extra degrees of freedom to the system to represent discontinuities.

The phantom node technique has several features that make it more attractive than the originally-proposed X-FEM for a Heaviside enrichment capability from an implementation standpoint:

- It is generally less invasive on a host FEM code architecture because it does not require the addition of nonstandard degrees of freedom, and requires only minor modifications to the element integration procedures.
- The additional degrees of freedom correspond to standard solution fields, which aids in interpretation of results.
- It simplifies the handling of crack branching and coalescence, which require additional degrees of freedom in elements containing multiple cracks in the original X-FEM, but can be handled by recursively cutting elements in the phantom node method [17,18].
- For multiphysics applications where the physics applications share a common mesh, the phantom node technique automatically enriches the degrees of freedom for all solution variables, whereas additional enrichment degrees of freedom would need to be explicitly added in the original X-FEM.

For these reasons, the phantom node method has been widely used to implement Heaviside-enriched X-FEM [19]. These reasons, in particular the advantages for multiphysics applications, also motivated its use as the basis of the X-FEM implementation in the present work. Although the phantom node method does not preclude inclusion of the near-tip enrichment term in Eq. (4), it is not considered in the present work for the sake of simplicity, and crack tips are required to coincide with element edges.

3.1. Mesh cutting algorithm

The bulk of the complexity in implementing the phantom node method lies in correctly resolving the connectivity of the partial elements that are created when elements are cut by a crack. Neighboring elements that share a common cracked edge should share physical and phantom nodes to ensure continuity of finite element solution fields in across neighboring elements in the material on a

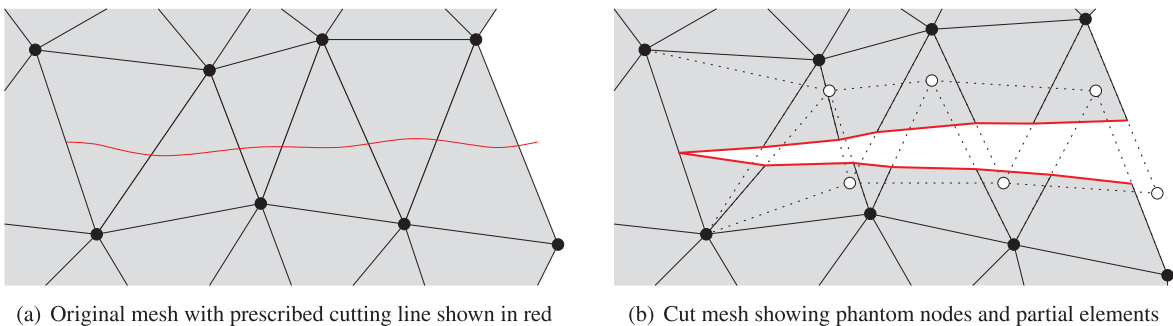


Fig. 1. Use of the mesh cutting algorithm to modify a mesh and with appropriate element connectivities for use with the phantom node algorithm to represent Heaviside discontinuities arising from a prescribed crack.

given side of a crack. Conversely, the elements on opposing sides of a crack should have no connectivity to ensure that the discontinuity is properly represented. Fig. 1 illustrates the desired connectivity for a representative crack geometry. An algorithm based partly on the work of Richardson et al. [18] was developed for the present work, and is described here. Because this cutting algorithm relies on the use of data structures known as “fragments”, it is termed here as the “element fragment algorithm” (EFA).

Fracture mechanics problems impose important requirements on the behavior of the cutting algorithm at crack tips. In general, the X-FEM permits a crack tip to be located anywhere in the solution domain, including within finite elements. If only Heaviside enrichment is used, however, crack tips must coincide with finite element boundaries. To properly represent the topology at crack tips, the cut edges of the partial elements representing the material on opposing sides of the crack must be merged with the uncut element ahead of the crack tip. This can be seen in Fig. 1. In addition, to represent cracks that propagate over time, as a crack advances into a new element, the merged edges of those elements that were previously at the crack tip must be disconnected.

This special handling of propagating cracks introduces additional complexity to the cutting algorithm. One could avoid this by simply discarding the cut mesh every time cracks advance and cut a copy of the original mesh. However, in simulations where stateful material data is associated with element integration points, it is important to not discard the cut elements, because they contain unique material data that would be lost if the cut mesh were deleted. For this reason, the algorithm described here is designed to operate on the cut mesh in its previous cut state every time the mesh is to be modified to extend existing cracks or initiate new cracks. This approach also has the advantage that it avoids the memory requirements of storing the uncut mesh.

3.1.1. Data structure and terminology

The EFA uses a mesh data structure that consists of elements connected by nodes, just like a finite element mesh. It does not explicitly require the nodal coordinates because it only deals with the connections between elements, and not the physical locations of those elements. An implementation of this algorithm could use the same finite element data structures used by the host code, but in the present work, a separate mesh is used for the EFA. This allows features specific to this algorithm to be added to the data structure without impacting the rest of the host finite element code.

Describing the EFA requires the definition of some unique terminology:

- **Cutting Plane:** These are geometric planes used to define locations of discontinuities represented by X-FEM. These can be defined in a number of ways, such as through simple geometric descriptions or level set functions. These can evolve as indicated by physics-based criteria such as stresses or fracture integrals that indicate how that cracks should extend.
- **Child Element:** Every element that is traversed by a cutting plane is replaced by multiple new elements, which are denoted as child elements.
- **Parent Element:** The elements that are replaced by child elements when traversed by cutting planes are known as parent elements.
- **Crack Tip Element:** Elements immediately ahead of the crack tip (which is represented by two partial elements that are both connected to the same uncut face of a neighboring element) are denoted as crack tip elements.
- **Crack Tip Split Element:** The partial elements just behind the crack tip that overlap another partial element that is merged with a common element face at the crack tip are called crack tip split elements.
- **Child Node:** As child elements are created to replace parent elements, some of the nodes in these child elements are new nodes that overlay existing nodes. These are known as child nodes.
- **Parent Node:** The nodes that are duplicated to give rise to child nodes are known as parent nodes.
- **Embedded Node:** These are additional nodes that are created at the intersections of cutting planes with finite element edges or other cutting planes. These nodes are globally numbered like standard finite element nodes, but are not associated with degrees of freedom in the discretized equation system. They are used for bookkeeping in the EFA.
- **Fragment:** The portion of a cut finite element representing the material located on one side of one or more cutting planes is known as a fragment. An element could potentially be cut by multiple cutting planes, and the fragments represent the smallest quantities of uncut material within an element. The union of the fragments in a given set of child elements completely covers the domain of their original parent element. Fragments are defined by the set of line segments that make up their perimeter in 2D or by the set of faces that make up their boundary in 3D. The line segments connect nodes, which can be either embedded nodes or permanent nodes (defined later). A new child element is created for each fragment in the parent element, and each child element contains exactly one fragment.
- **Temporary Node:** When child elements are created, new nodes are created at the locations of all nodes that are not contained within a fragment (i.e. connected to physical material). These new nodes are known as temporary nodes. These temporary nodes are ultimately merged with other nodes as connectivities are determined, and are either deleted or converted to become permanent nodes (defined later), so that after the EFA is complete, there are no remaining temporary nodes.
- **Permanent Node:** Permanent nodes are the finite element nodes that remain after the EFA is complete. These nodes may or may not be connected to physical material. All permanent nodes are associated with degrees of freedom in the global system of equations.
- **Phantom Node:** Phantom nodes are a subset of the physical nodes, and are the nodes not connected to any physical material. They are not actually handled any differently than other finite element nodes, and there is no need to designate nodes as being phantom nodes in the algorithmic implementation, but for understanding the EFA and its outcomes, it can be helpful to describe nodes as being phantom nodes.

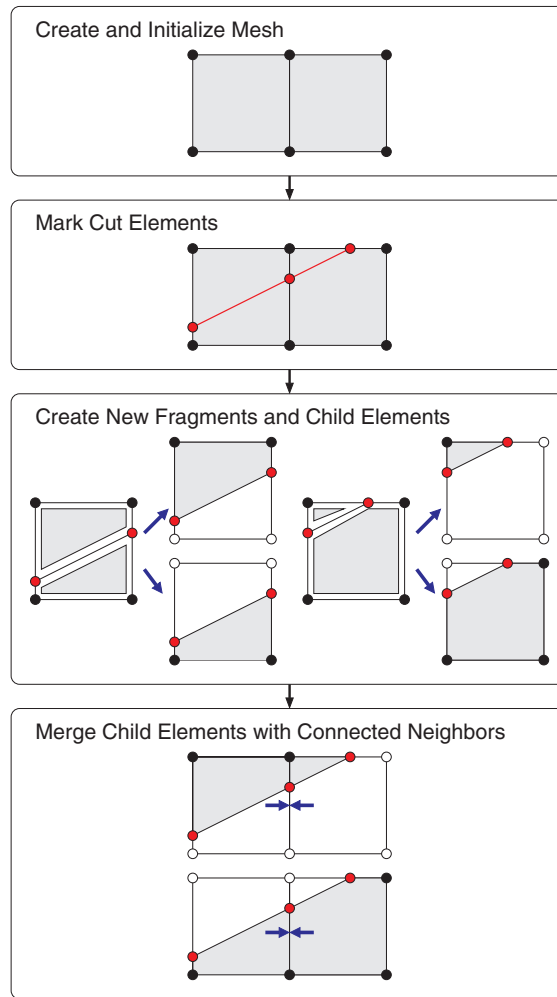


Fig. 2. High level flow chart illustrating the steps in the EFA.

3.1.2. Algorithmic flow

The EFA is designed to be called repeatedly during an analysis to represent dynamically evolving crack topologies. As illustrated in Fig. 2 and also outlined in [20], each time the mesh is to be modified, the following steps are taken:

1. **Create and Initialize Mesh:** The mesh structure for the EFA is populated with elements and nodes corresponding to those in the host code. If the mesh has been previously cut by the EFA, the topology of the cut mesh, rather than the original mesh is used. Any information about fragments and embedded nodes from the previous cut state is also restored. Neighboring elements connected to all elements in this cut mesh, as well as the current crack tip elements and crack tip split elements, are identified.
2. **Mark Cut Elements:** Elements newly intersected by cutting planes are identified, and new embedded nodes are created at the locations on the edges that are intersected. The determination of whether elements are cut and identification of locations of intersections of planes with element edges are performed in the host code. The embedded node locations are defined in the EFA in terms of the edges on which they are located and the fractional distances on those edges. The distances on the edges are necessary to disambiguate which embedded node corresponds to a cutting plane when multiple cuts intersect an element edge. This scenario is naturally handled by this algorithm, but is not discussed in detail here.
3. **Create New Fragments and Child Elements:** Once all cut elements are identified, new fragments are created for each continuous region within an uncut element, and a new child element is created corresponding to each fragment. Fig. 3 illustrates this process. New temporary nodes are created as children of the original nodes in the portions of the child elements outside of fragments, while the original permanent nodes are used when a node is contained within a fragment. Crack tip elements have one or more edge (in 2D) or face (in 3D) intersected by a cutting plane that terminates at, but does not traverse the element. These elements have a single fragment created, which contains the embedded node (2D) or nodes (3D), and a single new element is created corresponding to that fragment. The element on the far right of Fig. 4 is an example such an element.
4. **Merge Child Elements with Connected Neighbors:** The last phase of this algorithm is to merge the newly-created child elements

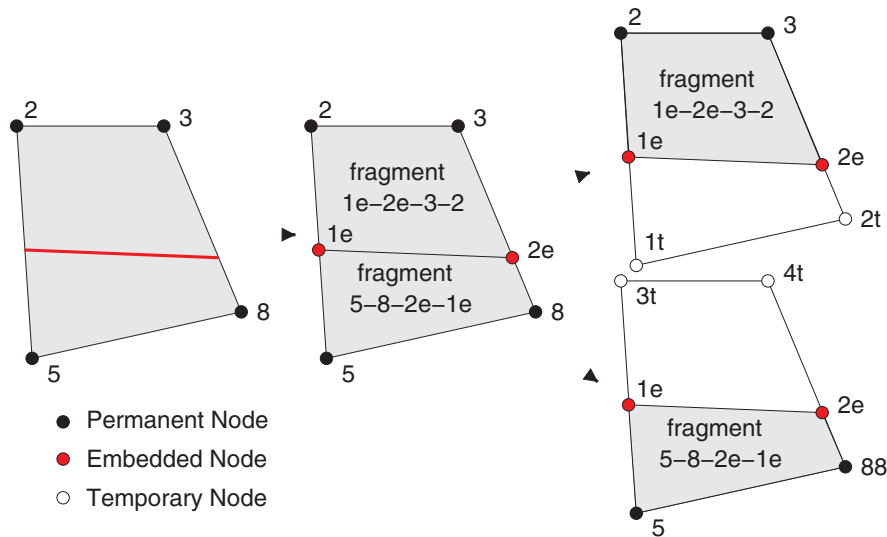


Fig. 3. Illustration of the process of marking and splitting an element. First, it is determined that the element is intersected by a cutting plane (left). Embedded nodes (denoted with an “e”) are then created at intersections of element edges with the cutting plane, and fragments are created for each continuous region within the cut element (middle). Fragments are identified by the set of edges defining their boundaries. Finally, a new child element is created corresponding to each fragment, with new temporary nodes (denoted with a “t”) to replace all nodes that are not connected to a fragment (right).

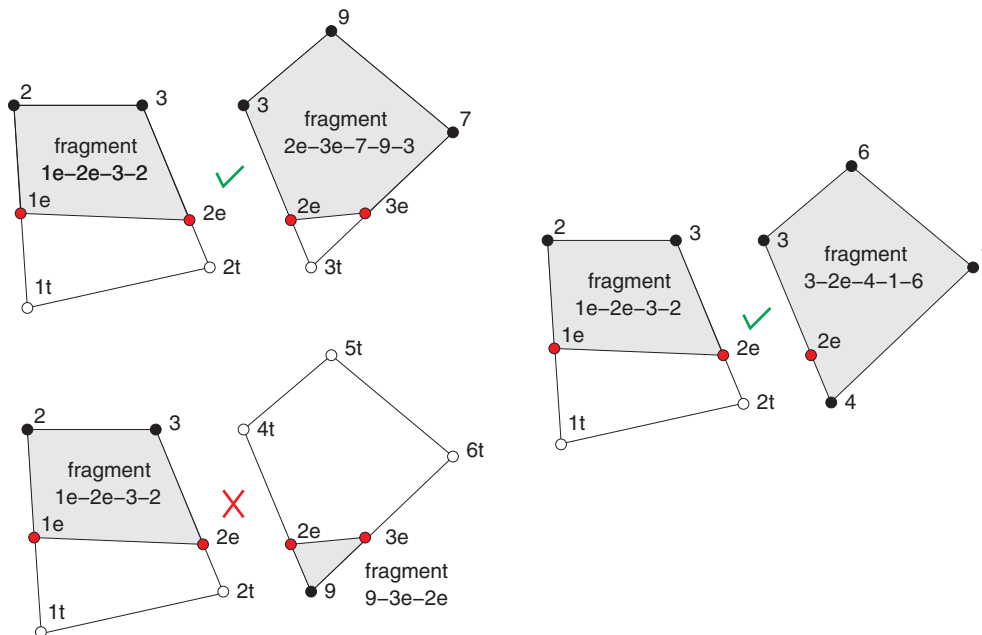


Fig. 4. Determination of whether two neighboring elements share a material connection and should be merged on a common edge. The two elements in the upper left are merged because their fragments share a common edge (3-2e). The fragments in the elements in the lower left do not share any common edges, so those elements are not merged. The scenario on the right shows how the crack tip split element on the left should be merged with a crack tip element on the right because their fragments share a common edge (3-2e).

with neighboring elements as appropriate, which is done by merging nodes on the common edge of the two elements. Neighboring elements are merged if they have a material connection, which means they share a common edge (2D) or face (3D) that has physical material connected to a common portion of it on both elements. The fragments are used for making this determination. If the fragments in two neighboring elements share a common edge (2D) or face (3D), the elements are deemed to have a material connection, and the nodes on the edge or face containing that connection should be merged. This ensures that there is spatial continuity in the solution variables in that region, as is appropriate for representing a continuous material.

A few rules are followed when merging nodes on common edges. If a temporary node is merged with a permanent node, it deleted

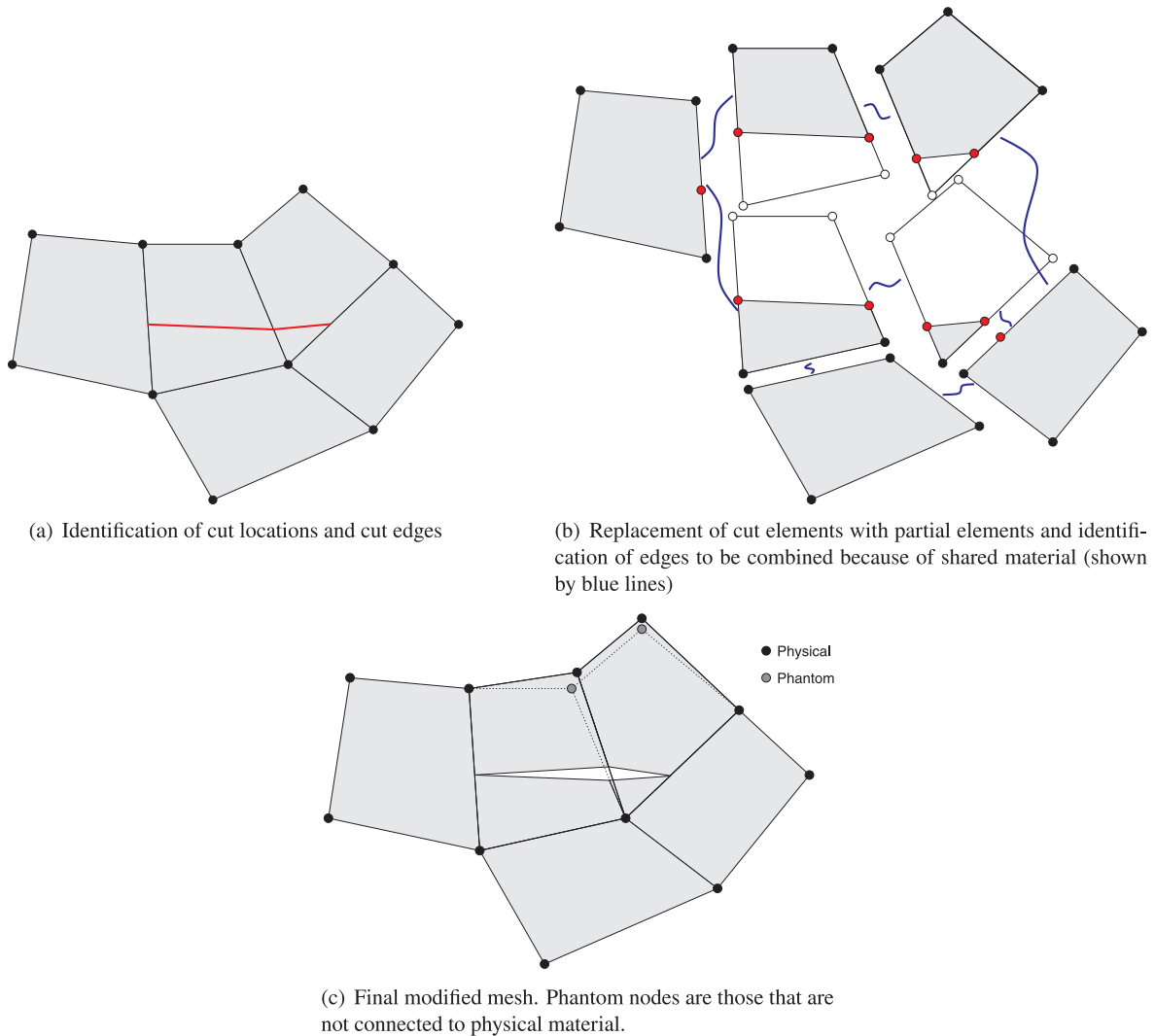


Fig. 5. The full process of the element fragment algorithm demonstrated on a patch of elements.

and replaced by the permanent node. If two temporary nodes are merged, they are both deleted and replaced with a single newly-created permanent node. Finally, there are some special scenarios in which two permanent nodes are to be merged and have differing indices. This can occur at nodes on the edge or face where a crack terminates if those nodes are also connected to another edge or face traversed by the crack behind the crack tip. In such cases, one of those nodes is always a child of the other node. The child node is deleted and replaced with the permanent node.

When this algorithm is completed, all temporary nodes should be deleted and replaced by permanent nodes. The EFA generates a set of new child nodes and a set of new child elements to be created, as well as a set of parent elements to be deleted. The new child elements and nodes are all associated with their parents, so that material data can be transferred to the child elements and nodal solution data can be transferred to the child nodes. Fig. 5 shows the full process of the EFA demonstrated on a patch of elements partially intersected by a cutting plane. The resulting mesh represents two crack tips at the ends of the cutting plane.

As mentioned previously, for this algorithm to permit the extension of cracks using the state of the mesh cut in a previous step, special treatment of the crack tip split elements is required to disconnect the nodes that were shared on the edge (2D) or face (3D) where the crack tip was previously located. In step 3 of the algorithm described above, elements that were previously split by a cutting plane are usually left alone, with no new fragments or child elements created. In the special case where a crack will fully cut a crack tip element, however, the crack tip split elements adjacent to that element each create a single new child element containing the same fragment that was present prior to this step. This results in the creation of new temporary nodes, which are merged with other nodes using the standard procedure.

Although the EFA is illustrated here using a 2D mesh and the applications shown in this paper are limited to 2D, this algorithm is readily applicable to 3D models. When there are distinctions between the 2D and 3D cases, those have been described in the above

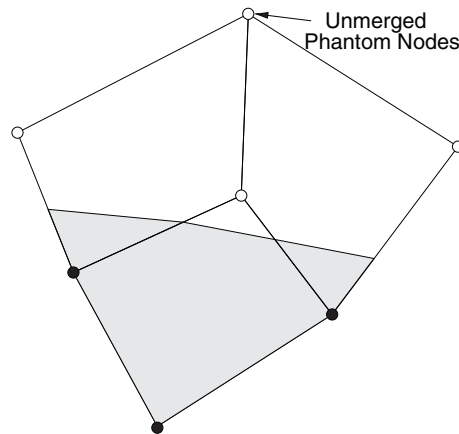


Fig. 6. Scenario in which the unmodified element fragment algorithm results in extra degrees of freedom. Without special treatment, there are two coincident phantom nodes at the indicated location because the neighboring edges share no physical material.

description of the algorithm, and these generally are related to the use of higher dimensionality geometric primitives (e.g. faces instead of edges) for the 3D case. Also, this is not directly an issue with the EFA, but when extending this approach to 3D, there are other challenges such as continuity of the cutting planes between adjacent cracked elements [21] that must also be addressed.

Finally, it should be noted that in the EFA as described above, if two child elements cut by the same crack have an edge that their parents share in common, but that edge contains no physical material, the nodes on that edge are not merged. This results in an extra phantom node, and hence an extra degree of freedom for every solution variable at that node. This behavior differs from the original XFEM, which would only add one degree of freedom to that node per field variable component. This scenario is shown on the patch of elements shown in Fig. 6. The MOOSE implementation of this algorithm provides an option to merge these edges to recover the original XFEM behavior, and this is used in the present work.

3.2. Partial element integration algorithm

Aside from the mesh cutting algorithm, the other major modification that must be made to the finite element code for the phantom node algorithm is that quadrature rules that are used to perform volume integrals, such as for computing the integral of the divergence of the stress tensor to compute an element's contribution to the residual, are adjusted to integrate over the physical portions of the cut elements. This is commonly done by forming a set of triangular (2D) or tetrahedral (3D) sub-elements that cover the entire physical portion of the split element's domain. These sub-elements are used only for integration, and new integration points are introduced at the locations of those sub-elements' integration points.

A significant drawback of this sub-division approach to partial element integration is that when there is stateful material data at integration points (as is often the case for nonlinear mechanical constitutive models and a variety of other behavior models used in fuel performance analysis), this data must be mapped to the new integration points. There are approaches to integration of partial elements that avoid this mapping of material data to new integration points by using the original integration points, but scaling the weight factors in the numerical integration procedure to give a reasonable approximation of the integration of a function over a portion of the domain. The simplest approach is to simply scale the weights by a factor equal to the physical volume fraction of a split element. A more sophisticated approach known as moment fitting uses a least squares procedure to compute separate weights for each integration point to optimally integrate a specified set of functions. A recent study by [22] shows on a variety of problems that the moment fitting approach gives results that are slightly improved over the simple volume fraction approach, and that both approaches are viable on problems of practical interest. The moment fitting scheme described in that work is used with a four-point integration rule for the 2D linear quadrilateral elements used in the present study.

3.3. Visualization of results

The mesh-cutting algorithm and the partial element integration scheme are the only major changes to a finite element code that are strictly necessary for an X-FEM implementation using the phantom node algorithm. However, because the phantom node approach replaces each cut element with overlapping elements, it is also very helpful during visualization to show only the physical portions of cut elements, as the non-physical portions of those elements can obscure the results of interest. It is important to note that in the phantom node approach, the actual displacement fields are directly computed, and there is no need to modify the visualized results beyond clipping the non-physical portions of cut elements to account for enrichment, as is necessary in the original X-FEM.

4. MOOSE/Bison X-FEM Implementation

Bison is a finite element based fuel performance code developed at Idaho National Laboratory (INL) to simulate the performance of a variety of nuclear fuel forms, including LWR fuel [4]. Bison is built on the open-source MOOSE multiphysics framework [23], which provides it the flexibility to include arbitrary coupled systems of partial differential equations (PDEs) describing the relevant physics models in a multidimensional setting. Bison fuel performance analyses typically include coupled thermal and mechanical physics, but because of the flexibility of its underlying multiphysics solution framework, it readily permits the inclusion of other physics that affect fuel performance, such as species diffusion.

While the primary motivation for the work described here was to add a mesh-independent discrete fracture capability to Bison for fuel fracture applications, this was accomplished by implementing the X-FEM in the MOOSE framework. As a result, this capability is available for use for any code based on MOOSE, including Bison. The MOOSE framework has a modular structure that provides pluggable interfaces that make it straightforward for an application to define additional physics models, such as additional terms in a PDE, material models, or additional field variables.

In choosing a strategy for implementing the X-FEM in MOOSE, it was important to consider the implications of this multiphysics environment. Rather than limiting the X-FEM solution enrichment to permit discontinuities in just one physics such as solid mechanics, the implementation was generalized to allow for enrichment of all of the solution variables in a given simulation. In thermal-mechanical fracture problems, which are the focus of the current paper, cracks introduce discontinuities in both the temperature and displacement fields, and the X-FEM implementation must have the flexibility to support that. Because the phantom-node-based X-FEM approach described here introduces discontinuities by modifying the mesh connectivity and integration of elements intersected by discontinuities, it can be applied generically to include discontinuities in a variety of systems of PDEs solved using the finite element method, which makes it very attractive for use within the MOOSE framework. Although the applications presented here are limited to thermal-mechanical problems, the X-FEM implementation in MOOSE is able to enrich all solution variables in a multi-physics simulation.

To visualize the results of MOOSE-based X-FEM simulations, a plugin for the open-source ParaView visualization software [24] called 'MooseXfemClip' was developed to clip off and hide the non-physical portions of cut elements. The data defining the geometric locations of the X-FEM interfaces used to clip individual elements is provided as field data in the standard results file generated by MOOSE. This plugin is used in the present work, and is now distributed along with its source code in the standard ParaView release.

5. X-FEM crack initiation and propagation

The X-FEM enriches the solution to include Heaviside discontinuities or crack tip fields given the location of discontinuities once those are defined, but does not by itself define the locations of those discontinuities. The applications in this paper include problems with pre-defined stationary cracks, problems with propagation from initially-prescribed cracks, and problems where cracks initiate and propagate. Both crack initiation and propagation are driven by the evolving mechanical physics solution. The techniques for determining whether and in which location cracks will initiate and propagate used in the present work are described here. Because the crack propagation technique is common to both the cases with initial prescribed cracks and those with cracks that initiate during the analysis, it will be described first, followed by the initiation technique.

5.1. Crack propagation

To determine the direction of crack propagation, the maximum hoop stress criterion is used, which states that the crack will propagate from its tip in a critical direction θ_c in which the hoop stress $\sigma_{\theta\theta}$ is maximized. Under general mixed-mode loading, the asymptotic near-tip hoop stress takes the following form:

$$\sigma_{\theta\theta} = \frac{K_I}{4\sqrt{2\pi r}} [3\cos(\theta/2) + \cos(3\theta/2)] + \frac{K_{II}}{4\sqrt{2\pi r}} [-3\sin(\theta/2) - 3\sin(3\theta/2)] \quad (5)$$

where K_I and K_{II} are the Mode-I and Mode-II stress intensity factors, respectively, and the location of the point relative to the crack tip is given in terms of the radial distance r and angle θ . The roots of the equation for θ_c are given as

$$\theta_c = 2\arctan \frac{1}{4} \left(\frac{K_I}{K_{II}} \pm \sqrt{\left(\frac{K_I}{K_{II}} \right)^2 + 8} \right) \quad (6)$$

The correct root of θ_c is chosen as the one which gives the larger hoop stress as computed in Eq. (5).

The stress intensity factors are computed using domain forms of the interaction integrals, which are a means to extract mixed-mode SIFs from the solution fields in models of fracture mechanics problems. With the finite element method, these integrals are normally calculated in a post-processing step as a domain integral over a finite sized volume in the vicinity of a point on the crack front. The integrand involves a combination of fields from the finite element approximation and auxiliary fields from asymptotic solutions for fracture problems. The interaction integral at location s along a 3-D crack front can be written as [25]:

$$I(s) = \int_V [\sigma_{ij} u_{j,1}^{\text{aux}} + \sigma_{ij}^{\text{aux}} u_{j,1} - \sigma_{jk} \epsilon_{jk}^{\text{aux}} \delta_{il}] q_i dV \quad (7)$$

where σ is the stress, u is the displacement, and q is a weight function that represents the field of virtual displacements due to the virtual crack extension. The q function is set to be 0 for the nodes that are inside an inner ring and 1 outside an outer ring. If the selected ring radii are large enough to be outside the region of strong singularity near the crack tip, and the mesh is sufficiently refined the computed integrals are independent of the ring radii. In the examples in this study, the radii of the inner and outer ring are chosen as $1.5h$ and $3.5h$, respectively, where the h is average element size. By expressing the energy release rate in terms of the mixed-mode stress intensity factors, the interaction integral evaluates to:

$$I(s) = \frac{1 - \nu^2}{E} (2K_I K_I^{\text{aux}} + 2K_{II} K_{II}^{\text{aux}}) + \frac{1 + \nu}{E} (K_{III} K_{III}^{\text{aux}}) \quad (8)$$

To obtain individual stress intensity factors, the interaction integral is evaluated with different auxiliary fields. For instance, by choosing $K_I^{\text{aux}} = 1.0$ and $K_{II}^{\text{aux}} = K_{III}^{\text{aux}} = 0$ and computing $I(s)$ in Eq. (7), K_I can be solved for in Eq. (8).

Whether a crack should propagate after it nucleates is determined by the failure criterion given as:

$$K_c \leq \sqrt{(K_I^2 + K_{II}^2)} \quad (9)$$

where K_c is the critical stress intensity factor. The cracks are extended if this propagation criterion is met, and the solution for the current step is repeated after extending the cracks until the crack propagation condition is no longer met for any cracks. If the propagation criterion is met for a crack, it is extended either by a constant prescribed length or an entire element, as determined by the user. The crack growth over a time step is an accumulation of potentially multiple extensions that have been made during the process of iteratively extending the crack and repeating the step. With a sufficiently refined mesh, this becomes non-sensitive to the choice of crack incremental growth length.

5.2. Crack initiation

Many applications of the X-FEM involve evaluations of pre-defined cracks, in which case there is no need for a criterion for crack initiation. However, many other problems of interest, such as the nuclear fuel problem considered here, involve both crack initiation and propagation. Developing a reliable criterion for crack initiation for use with the X-FEM can be challenging, and the most common approach is to place a crack at the location of maximum stress when a stress criterion is exceeded.

In a cylindrical fuel pellet subjected to a power ramp or steady-state power, the highest stresses in the uncracked pellet occur on the outside surface of the fuel due to the nonuniform thermal expansion caused by elevated temperatures on the pellet interior relative to the exterior. In the present work, this is exploited to simplify the approach for modeling crack initiation, and cracks are permitted to initiate only on the outer surface of the fuel. The finite elements adjacent to the exterior boundary are checked to see whether the maximum hoop stress exceeds a critical value. If the criterion is met in a given element, a crack is initiated by cutting through the element in the direction normal to the hoop stress.

Before cracking occurs in an uncracked cylindrical fuel pellet, if there is no azimuthal variation in the power or other relevant conditions, and there is also no azimuthal variation in the stress state. Because the hoop stress is uniform around the periphery of an idealized pellet, cracks would simultaneously initiate at every element around the pellet exterior once the critical hoop stress criterion is met. In an actual fuel pellet, however, a limited number of cracks would initiate where local defects are present. In the present study, a random distribution of the local fracture strength is introduced with the goal of initiating a realistic, limited number of localized cracks in the simulations. In addition, the effect of specimen size on the fracture strength should be taken into account to mitigate mesh size dependencies [26–28]. This size effect is due to the fact that a larger material specimen is likely to contain more flaws than a smaller one. In finite element models, larger finite elements represent larger volumes of material, so to minimize mesh size dependencies, they should also have a higher probability of failure.

In this study, following the work of [27], a randomized, size-dependent fracture strength is assigned to each finite element of volume V using a volume-corrected Weibull distribution as:

$$\eta = \bar{\eta} \left[\frac{\bar{V} \ln R}{V \ln(1/2)} \right]^{1/m} \quad (10)$$

where η is a randomized material property (fracture strength, in this case), $\bar{\eta}$ is the median value of η observed in the laboratory using a specimen of volume \bar{V} , R is a uniformly-distributed random number on the interval between 0 and 1, and m is the Weibull modulus.

To demonstrate the effect of mesh size on the randomly generated fields using this approach, fields were generated on a series of meshes, and the number of elements having values below a median value was computed on each mesh. This was done on a set of irregular meshes of a 2D circular domain with a radius of 1, using a Weibull modulus $m = 15$ and a median value $\bar{\eta} = 100$ with a reference volume $\bar{V} = 0.1$. Fig. 7(a) shows one realization of perturbed properties assigned to elements as defined by Eq. (10). Fig. 7(b) shows that as element size decreases, the number of elements with η below the prescribed median value of 100 approaches a constant value. Because brittle fracture behavior is largely driven by the number of weak points, this implies that this approach would minimize mesh size dependencies if the mesh is sufficiently fine.

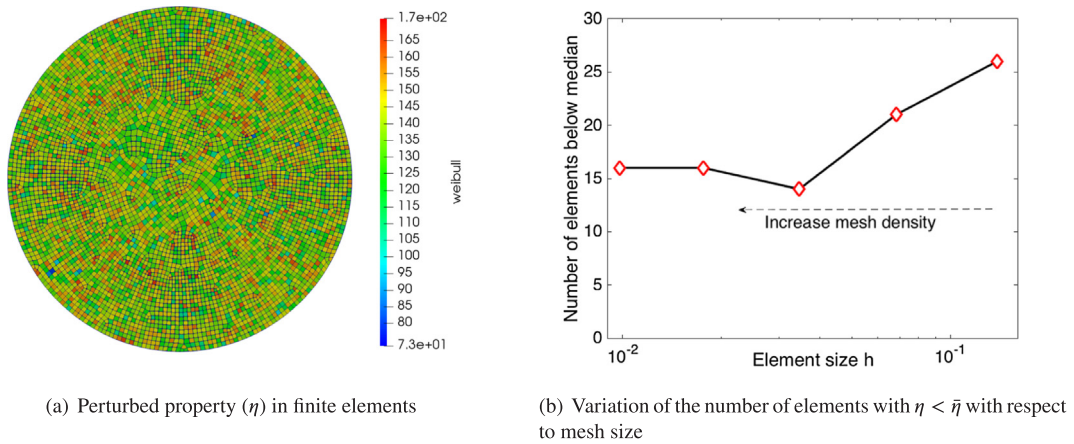


Fig. 7. Study of the effect of mesh density on the Weibull distribution.

6. Numerical examples

6.1. Rectangular plate with an inclined crack

We first consider an inclined crack to benchmark this thermo-mechanical X-FEM approach under mixed-mode conditions against published solutions. This example, shown in Fig. 8, is a rectangular plate under plane strain conditions containing an inclined crack, subjected to a temperature gradient. The plate has dimensions of $W = 1$ and $L = 0.5$. Temperatures of T and $-T$ are prescribed at the top and bottom surfaces, respectively. The finite element mesh, shown in Fig. 8(b), consists of a regular grid of approximately 11,000 elements with an element size $h \approx 0.13$. Two sets of parameter studies were performed. In the first study, we fix the angle of crack inclination $\theta = 30^\circ$ and vary the crack length of a from 0.2 to 0.6. In the second study, we fix the crack length $a = 0.3$ and vary the angle of inclination θ . Fig. 9 shows the temperature field for the case where $a/W = 0.2$ and $\theta = 30^\circ$. In Tables 1 and 2, we compare the our computed SIFs with those reported for the same problem by [29–31]. The reported SIFs are normalized by $\alpha T(W/L)E\sqrt{2W}$, where α is the thermal expansion coefficient and E is the Young's modulus. This comparison shows good agreement between the current approach and published results for both varying crack lengths and varying angles of inclination.

6.2. Crack propagation in a cruciform plate

In the second example, we demonstrate the ability of the thermo-mechanical X-FEM to represent crack propagation under mixed-mode loading on a cruciform specimen subjected to thermal and mechanical loading that has been studied by other authors. The geometry and boundary conditions are shown in Fig. 10(a). The length L is chosen as 10 cm and an initial crack with length of $0.2L$ is placed at one of the re-entrant corners. As shown in Fig. 10(b) a uniform regular mesh with element size $h = 0.2$ is used. Two different cases are considered with differing boundary conditions. In the first case, which is driven by primarily thermal loading, we apply $T = 100^\circ\text{C}$ and $T = -100^\circ\text{C}$ at the top and bottom surfaces, respectively and zero traction at the top surface. In the second case with only mechanical loading, we apply a traction $F = 10$ Pa at the top surface and zero temperature $T = 0^\circ\text{C}$ on all boundaries. The material properties used in this example are Young's modulus = 218400 Pa, Poisson's ratio = 0.3 and thermal expansion coefficient = $1.67 \times 10^{-5}\text{C}^{-1}$. The crack is grown by a constant length $\Delta a = 0.6$ cm. The critical stress intensity factor K_c is taken as 1 Pa

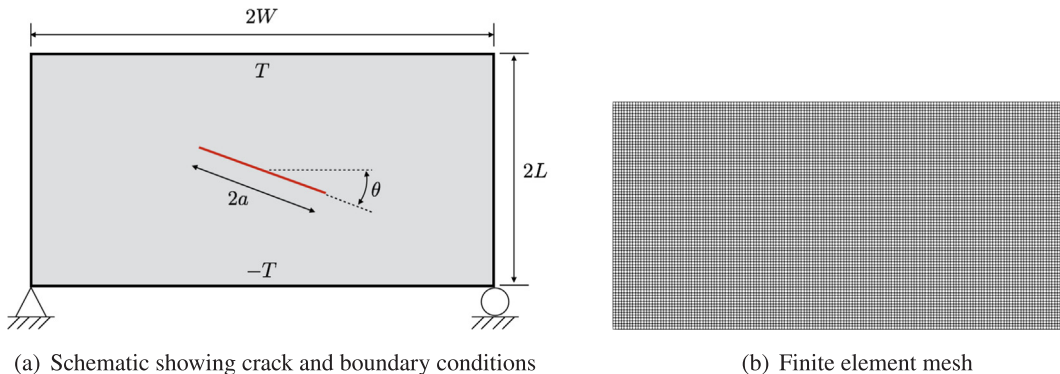


Fig. 8. Rectangular plate with an inclined crack.

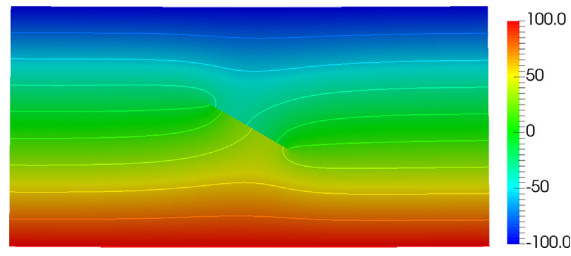


Fig. 9. Temperature for the inclined crack with $a/W = 0.2$ and $\theta = 30^\circ$.

Table 1

Normalized SIFs for the rectangular plate with an inclined crack with $\theta = 30^\circ$ and varying a/W . Results from the present study using X-FEM (“MOOSE”) are compared with those from other studies as indicated.

$\frac{a}{W}$	K_I				K_{II}			
	MOOSE	[29]	[30]	[31]	MOOSE	[29]	[30]	[31]
0.2	0.0020	0.0020	0.002	0.002	0.0283	0.0302	0.030	0.030
0.3	0.0067	0.0068	0.006	0.008	0.0470	0.0489	0.048	0.048
0.4	0.0149	0.0149	0.014	0.015	0.0626	0.0650	0.064	0.064
0.5	0.0264	0.0265	0.026	0.027	0.0753	0.0774	0.076	0.076
0.6	0.0410	0.0407	0.040	0.041	0.0854	0.0878	0.087	0.086

Table 2

Normalized SIFs for the rectangular plate with an inclined crack with $a/W = 0.3$ and varying θ .

θ	K_I				K_{II}			
	MOOSE	[29]	[30]	[31]	MOOSE	[29]	[30]	[31]
0°	0.0000	0.0000	0.0000	0.0000	0.0527	0.0546	0.054	0.054
15°	0.0038	0.0038	0.0036	0.0038	0.0513	0.0533	0.054	0.054
30°	0.0067	0.0068	0.0064	0.0071	0.0470	0.0489	0.048	0.048
45°	0.0074	0.0076	0.0071	0.0077	0.0385	0.0420	0.041	0.042
60°	0.0054	0.0054	0.0049	0.0053	0.0312	0.0322	0.032	0.032
75°	0.0018	0.0017	0.0010	0.0023	0.0174	0.0180	0.018	0.018
90°	0.0000	0.0000	0.0003	0.0000	0.0000	0.0000	0.000	0.000

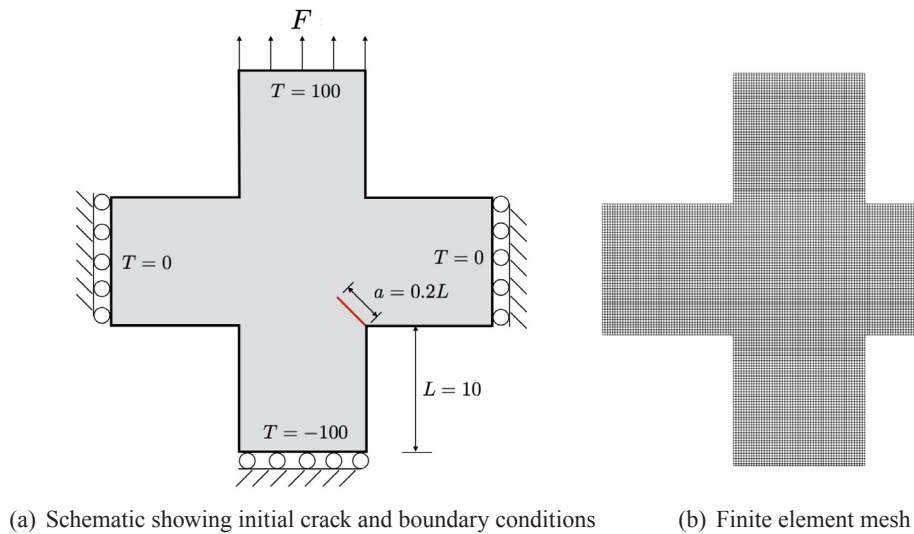


Fig. 10. Crack propagation in a cruciform plate.

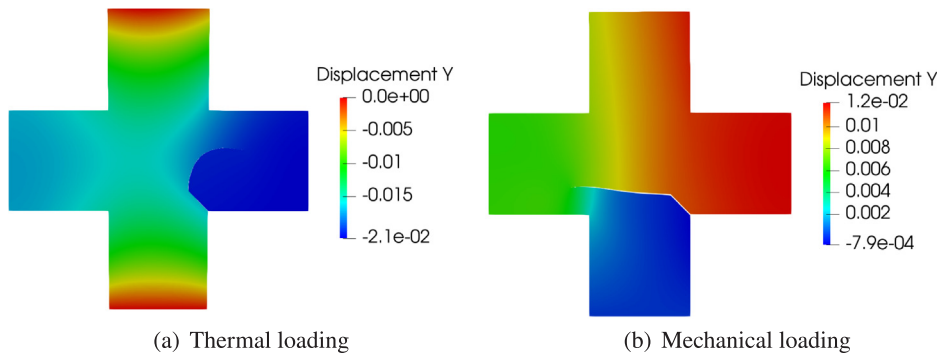


Fig. 11. Crack propagation paths predicted by thermo-mechanical X-FEM in a cruciform plate for two different loading cases. The contour shows the displacement (cm) in Y direction. (displacements are magnified $10\times$).

\sqrt{cm} . The direction of crack propagation is determined by the maximum circumferential stress criterion discussed in Section 5. As shown in Fig. 11, the crack paths for two boundary conditions are quite different. They agree well with those reported in [29,32].

6.3. LWR fuel pellet cracking

The first two examples have demonstrated the ability of the MOOSE-based X-FEM implementation to model stationary and propagating fractures under mixed-mode loading conditions induced by thermal and mechanical loading, with good comparison to benchmark results. This provides confidence in the applicability of this technique to model thermally driven fracture in LWR fuel, the study of which is the goal of this effort.

To demonstrate the use of the X-FEM to model LWR fuel pellet cracking, we consider a 2D generalized plane strain model of a fuel pellet. The generalized plane strain condition computes a uniform out-of-plane strain that results in a zero net out-of-plane force. The problem is designed to represent the conditions in fresh fuel subject to a ramp to full power. To simplify this problem, only the fuel pellet is modeled, without the cladding. In LWR fuel, the temperature on the fuel outer surface is strongly affected by the size of the gap between the fuel and cladding, which is constantly evolving due to the mechanical response of the system. To obtain a reasonable approximation of this temperature that can be applied as a boundary condition to a fuel-only model, a full Bison simulation including both fuel and cladding was run through the power ramp, and the time history of fuel outer temperature was applied as a boundary condition in the fuel-only model. This is the same procedure followed in [7], and the same temperature history used there is used in this study.

The fuel pellet has an outer radius of 0.41 cm and is meshed using 30,231 linear quadrilateral finite elements. All simulations assume a Young's modulus of 2×10^{11} Pa, a Poisson's ratio of 0.345, a thermal expansion coefficient of $10 \times 10^{-6} \text{ K}^{-1}$, and a constant thermal conductivity of 5.0 W/(m K). Spatially uniform volumetric heating is applied. The power is ramped up from zero to a linear power of 25 kW/m over 10000 s, and then held at that level. At this slow ramp rate, time-dependent effects are very minimal. More realistic models are available in Bison for a number of aspects of fuel system, and can be readily incorporated in an X-FEM fracture simulation, but this model is intentionally kept simple, as its intent is primarily to demonstrate this capability. This model with these boundary conditions is used to consider stationary and propagating cracks in the following sections.

The tensile strength and fracture toughness (K_{Ic}) of UO_2 are highly dependent on the characteristics of its microstructure. Tensile strength values reported by [33] vary from roughly 50 to 100 MPa, while those reported by [34] vary from roughly 60 to 160 MPa. Experimental fracture toughness (K_{Ic}) data for sintered UO_2 based on indentation testing have been reported by multiple authors. In a study using micro-indentation, K_{Ic} was reported in the range from 0.88 to 1.20 $\text{MPa}\sqrt{\text{m}}$ for UO_2 , showing dependence on porosity [35]. A more recent study by [36] based on nano-indentation of UO_2 with varying grain size reports values of K_{Ic} ranging from 1.0 to 1.3 $\text{MPa}\sqrt{\text{m}}$. The study of [37] evaluated tensile strength and K_{Ic} using indentation and bending tests, and considered both fresh and irradiated fuel. That study reported tensile strength values ranging from about 80 to 150 MPa, and K_{Ic} values ranging from about 0.8 to 3.2 $\text{MPa}\sqrt{\text{m}}$ for fresh fuel.

Based on the literature data summarized above, the tensile strength of UO_2 is assumed in the present work to be nominally 130 MPa, and K_{Ic} is assumed to be nominally 2 $\text{MPa}\sqrt{\text{m}}$. There is clearly a need to study the effects of these parameters, which can evolve significantly over the life of LWR fuel, on its fracture response, but a detailed study of this is outside the scope of this paper.

6.3.1. Stationary cracks in an LWR fuel pellet

Increasing the power in LWR fuel can result in the propagation and nucleation of multiple radial cracks. The stress field in the vicinity of a given crack is influenced by the presence of other cracks, so the interactions between cracks are important in determining whether a power ramp will result in propagation of existing cracks or nucleation of new cracks. This has important implications on the resulting fracture patterns and fuel relocation, as well as on the size distribution of fuel fragments, which is important for characterizing fuel behavior during accident conditions.

To quantify the effects of crack length and the presence of multiple cracks on the driving forces for propagation of radial cracks in

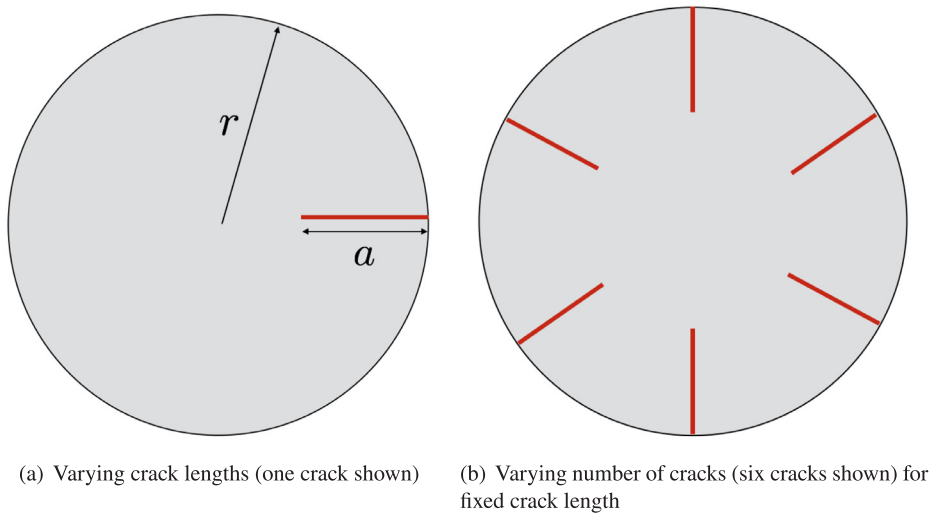


Fig. 12. Two scenarios for evaluation of SIF on stationary cracks in a 2D model of a cylindrical fuel pellet.

LWR fuel, we studied stationary cracks of varying number and length. Fracture integrals were evaluated to obtain the SIF on prescribed stationary radial cracks as shown in Fig. 12. The finite element mesh is shown in Fig. 13. Three cases with varying parameters were investigated during a ramp up to full power. In the first case, a single crack was considered, and the effect of varying its length was quantified. The crack length is quantified here by its normalized length, expressed as a/r , where a is the crack length and r is the fuel pellet radius. In the second case, the crack length was fixed at $a/r = 0.5$ and the number of cracks was varied. In the third case, both the crack length and the number of cracks are varied.

The SIF at the end of this same power ramp is plotted for a single crack with varying length in Fig. 14(a). The SIF initially increases with increasing crack length, but reaches a maximum value at $a/r \approx 0.42$. Further increasing the crack length beyond that point decreases the SIF significantly. This is because the temperature profile causes tensile hoop stresses on the pellet exterior, and compressive hoop stresses in the interior, so the crack eventually reaches a region of compressive stress. The radial position of the crack tip at the peak SIF is close to the point where the hoop stress transitions from a positive to a negative value as shown in Fig. 14(b).

Next, we study the effect of the presence of multiple cracks on the SIF by varying the number of radial cracks with a fixed length ($a/r = 0.5$). The results of this study are shown in Fig. 15 at the end of the same power ramp considered previously. The presence of other cracks decreases the constraint on the outside of the pellet and reduces the average hoop stress at a given radius, which reduces the SIF at the crack tips. It can be seen that the SIF decreases exponentially with an increasing number of cracks, so that by the time that there are five or six cracks, the SIF is an order of magnitude lower than it is for a single crack. At this point, adding more cracks

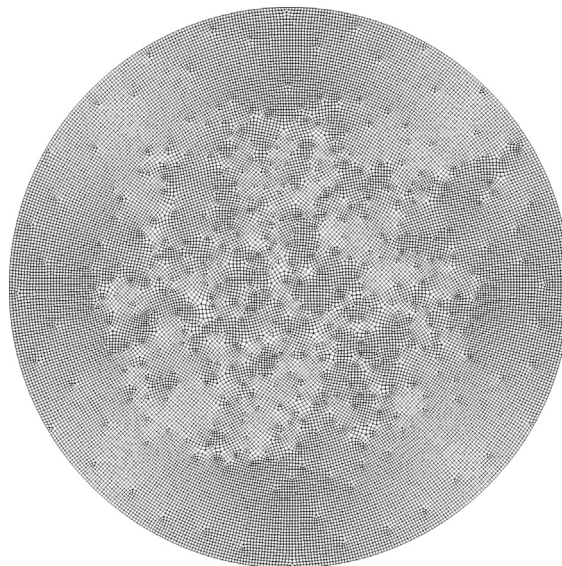


Fig. 13. Finite element mesh of the fuel pellet.

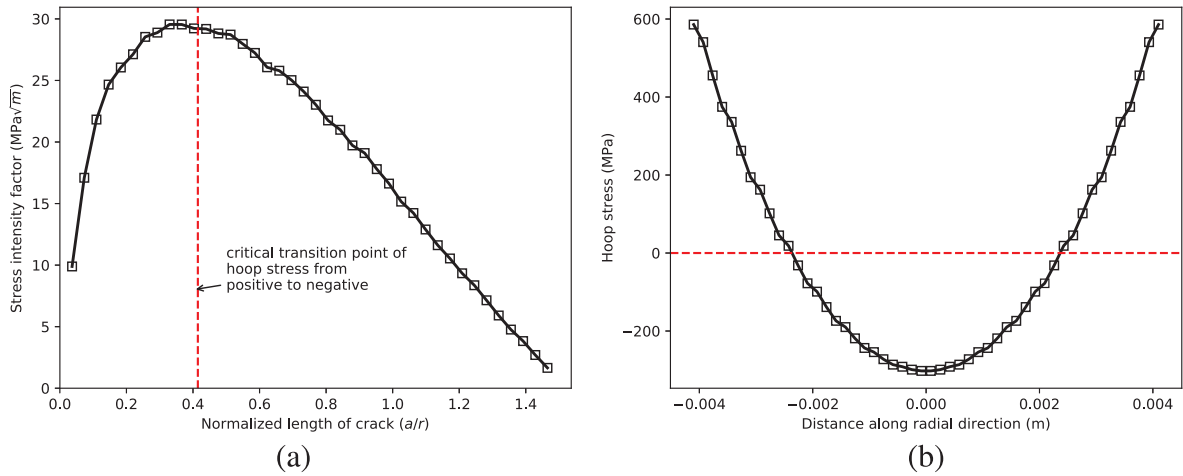


Fig. 14. (a) SIF as a function of varying normalized crack length at the end of the power ramp for a single stationary radial crack in an LWR fuel pellet. (b) Variation of hoop stress along line through the center of the pellet (in an uncracked pellet).

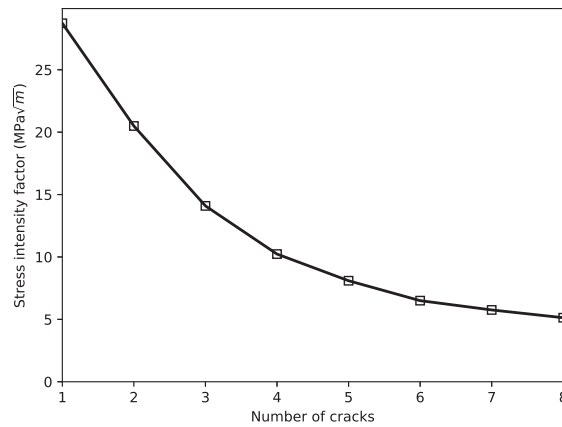


Fig. 15. SIF for varying number of radial cracks with a fixed normalized length of $a/r = 0.5$ at 10000 s.

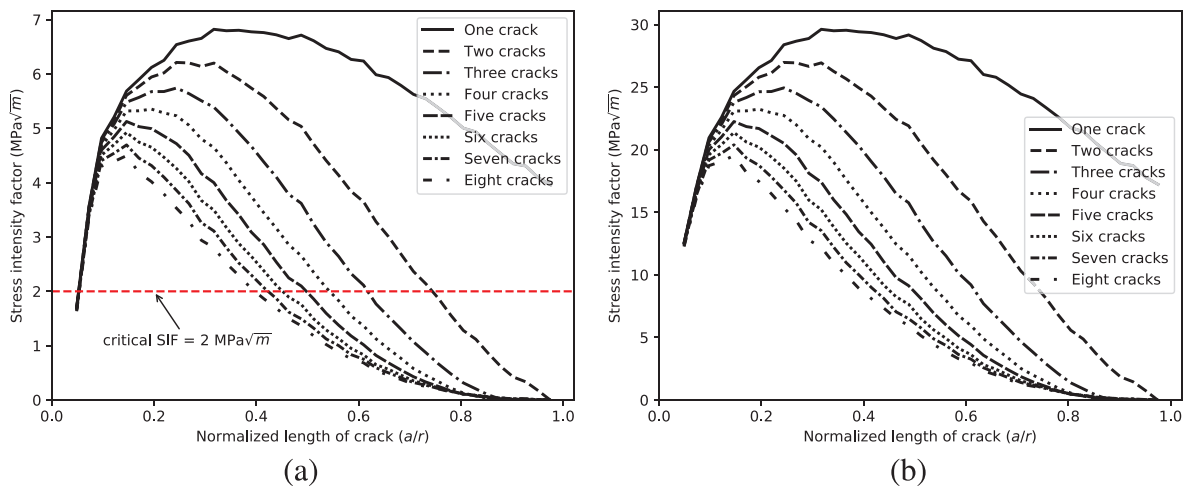


Fig. 16. Stress intensity factor as a function of normalized crack length for groups of varying numbers of radial cracks having the same length (a) time = 2300 s, power = 5 kW/M (b) time = 10000 s, power = 25 kW/M.

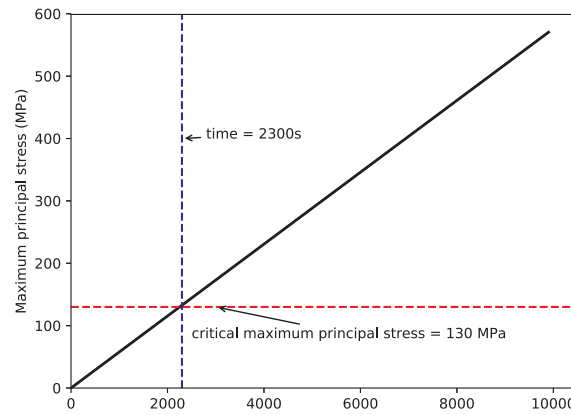


Fig. 17. Time history of maximum principal stress at the outer surface of the fuel pellet. The horizontal line corresponds with the nominal tensile strength, which occurs at a time of approximately 2300 s, which is the time at which the SIF plots are shown in Fig. 16(a).

does not significantly decrease the SIF.

Finally, we expanded on the study on the effect of length of a single crack shown in Fig. 14(a) by varying the lengths of set of cracks, all having the same length. The two plots in Fig. 16 show the stress intensity factor as a function of crack length for varying numbers of radial cracks from one to six together on a single plot at two different points in time during the same ramp to full power. Fig. 16(a) shows these results at a power of 5 kW/m, while Fig. 16(b) shows the results at a power of 25 kW/m. At higher powers, the family of curves has essentially the same shape, but is scaled up. The plot in Fig. 16(a) is of particular interest because this is a power level just below that at which cracks are expected to initiate.

These plots illustrate how when thermal stresses cause the stress intensity to exceed the material's toughness, either initiating additional cracks or propagating existing cracks can reduce the SIF until a stable equilibrium state is reached. If there are multiple cracks, the reduction in constraint due to the presence of the other cracks reduces the loading on the other cracks, and the stress intensity factor will decrease below the critical value for significantly smaller crack lengths. Equilibrium can be reached with varying numbers of cracks, and the presence of local defects will strongly influence fracture patterns in individual fuel pellets. The final number of cracks at a given power level depends heavily on the number of cracks that initiated and were large enough to have stress intensity factors above a critical value. Crack initiation is expected to occur primarily at the outer surface of the pellet where the tensile stresses are the highest. Fig. 17 shows the time history of the maximum principal stress at the outer surface of an uncracked fuel pellet to help understand when crack initiation will occur.

It is also important to note that although extending the length of a set of cracks will decrease the driving forces for propagation of those cracks, it may not relieve the stresses at other locations around the pellet's periphery sufficiently to prevent initiation of new cracks. This effect is evident in the plotted values of the stress intensity factor in Fig. 16, which show little interaction effects at low crack lengths. This is a strong contributor to the tendency for localization of several cracks, which has been observed in both experiment [3] and fracture propagation simulations [7–9].

6.3.2. Propagating cracks in an LWR fuel pellet

The major goal of this work is to predict the propagation of discrete cracks in a nuclear fuel pellet in a computationally efficient manner. The same fuel pellet model used to study on stationary cracks in the previous section is now used here to demonstrate the use of X-FEM to simulate crack initiation and propagation.

In this case, no initial cracks are prescribed, and cracks are permitted to initiate in elements adjacent to the exterior boundary of the fuel pellet if their maximum principal tensile stress exceeds the tensile strength of the material, taken to be 130 MPa here. When cracks initiate, they are given an initial length of 0.4 mm, which is a decision driven by the finite element mesh density, because the cracks must be sufficiently long to permit evaluation of fracture integrals. Once the cracks initiate, fracture integrals are evaluated at the individual crack tips, and the cracks are allowed to grow if the stress intensity factor exceeds a critical value. If this threshold is exceeded, the cracks are incrementally grown in one solution solve by a constant length $\Delta a = 0.2$ mm. If any cracks are initiated or extended, the solution for that time step is re-computed, and the XFEM crack topology is modified if the fracture criteria are still exceeded. This is repeated as many times as needed until the fracture criteria are no longer exceeded. Two separate simulations were run, using critical stress intensity factors of 2 and 4 MPa $\sqrt{\text{m}}$ to demonstrate the sensitivity to that parameter.

Eq. (10), is used to provide a local randomized strength factor η for each element. The mean strength factor $\bar{\eta} = 1.0$, and the locally sampled value for η is multiplied by the nominal material tensile strength and critical stress intensity factor for use in the local determinations of crack initiation and growth. The Weibull modulus m is taken to be 15, and the characteristic volume \bar{V} is taken to be average element volume of 1.74688 mm³ (based on a unit out-of-plane dimension of this 2D model).

These values, as well as the criterion for fracture propagation, were chosen because they are reasonable for ceramic materials. However, it is important to emphasize that there is currently very limited experimental data available to validate these models. In our experience, fracture propagation in LWR fuel is relatively insensitive to the fracture growth criteria simply because radial cracks tend

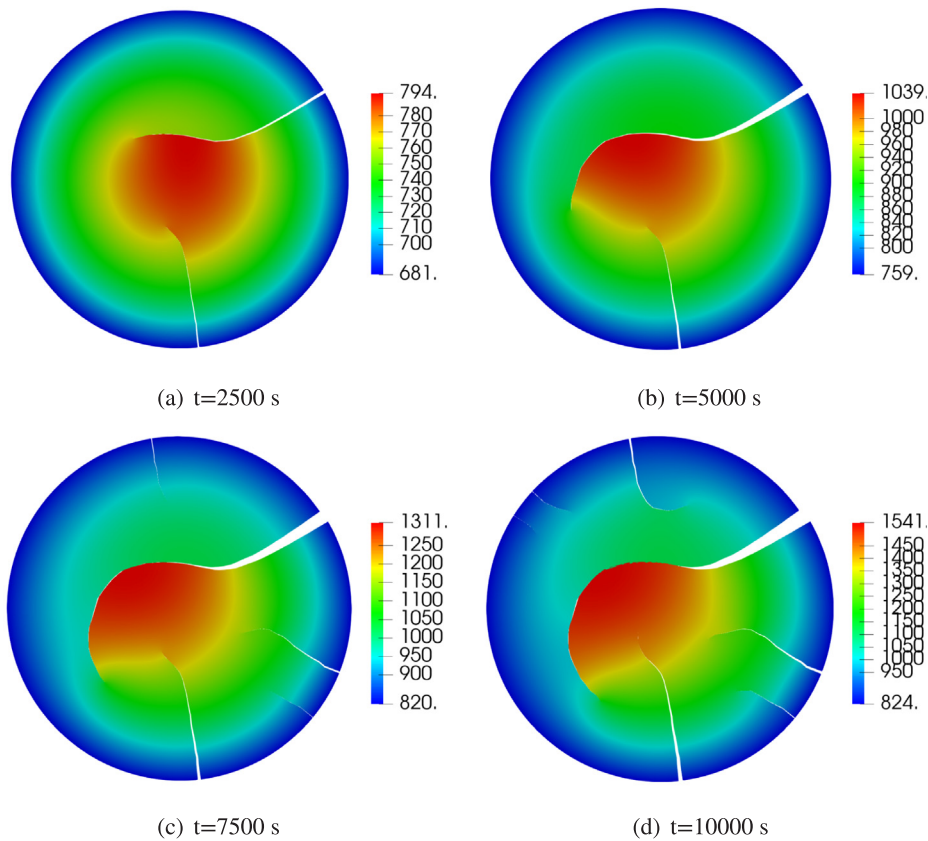


Fig. 18. X-FEM simulation results with critical stress intensity factor of $2 \text{ MPa} \sqrt{\text{m}}$ at selected times during power ramp showing displacements (magnified $5\times$) and temperature contours (K).

to propagate inward until they reach a compressive region. The present work includes a rudimentary study on the sensitivity of these models to some of these parameters, but a more thorough parameter study, as well as experimental data for validation, are important for gaining confidence in this model.

Fig. 19 shows the evolution of the cracking pattern with contours of the temperature field at several times during the same power ramp applied previously in the stationary crack cases with a critical stress intensity factor of $2 \text{ MPa} \sqrt{\text{m}}$. Similar results are shown for a critical stress intensity factor of $4 \text{ MPa} \sqrt{\text{m}}$ in Fig. 18. As the power increases, the interior temperature increases relative to the exterior, resulting in higher tensile hoop stresses on the outside of the pellet and corresponding compressive hoop stresses in the interior. This leads to initiation of many small cracks on the outer boundary.

Once these cracks initiate, some of them propagate radially inward as the power increases when their SIFs exceed the critical value. When there are multiple cracks in close proximity, extension of one of them decreases the driving forces for the other cracks in the vicinity, causing localization to occur. This process is numerically aided by the use of the randomized strength, which minimizes the potential for neighboring cracks to reach their extension criterion simultaneously. The roughly equal spatial distribution of the macroscopic cracks is a manifestation of this localization behavior. With a critical stress intensity factor of $2 \text{ MPa} \sqrt{\text{m}}$, one or two cracks tend to propagate rapidly toward the center of the fuel pellet as soon as they initiate. As they reach the center of the pellet, the cracks start to interact, causing curved crack paths. With a critical stress intensity factor of $4 \text{ MPa} \sqrt{\text{m}}$, the first cracks did not propagate as far into the center of the pellet when they first initiated, resulting in a larger number of cracks that followed straighter paths. The formation of five or six major radial cracks is consistent with crack patterns observed in [7,9].

A sensitivity study was conducted to investigate the effect of initial crack length and incremental crack extension length on the simulation results based on the model with a critical stress intensity factor of $4 \text{ MPa} \sqrt{\text{m}}$. The initial crack length must be larger than the outer radius used by the fracture domain integrals to calculate the SIFs. Three different initial crack lengths: 0.4 mm, 0.5 mm and 0.6 mm, were used. For each initial crack length, three values of the crack extension length: 0.20 mm, 0.25 mm and 0.30 mm, were used. The final cracking patterns for the 9 cases in this study, which all used the same realization of the randomized strength, are shown in Fig. 20. These results show that the solution is generally insensitive to the incremental crack extension length as long as this value is relatively small. This is expected because of the process of iteratively repeating the solution and growing cracks until the fracture criterion is no longer met. The choice of initial crack length, however, has a major effect on the cracking pattern. This is intuitive, because longer cracks result in higher stress intensity factors (as was demonstrated in Fig. 14), which makes them more likely to propagate soon after they are initiated. This would tend to cause localization of a smaller number of cracks, as was seen in

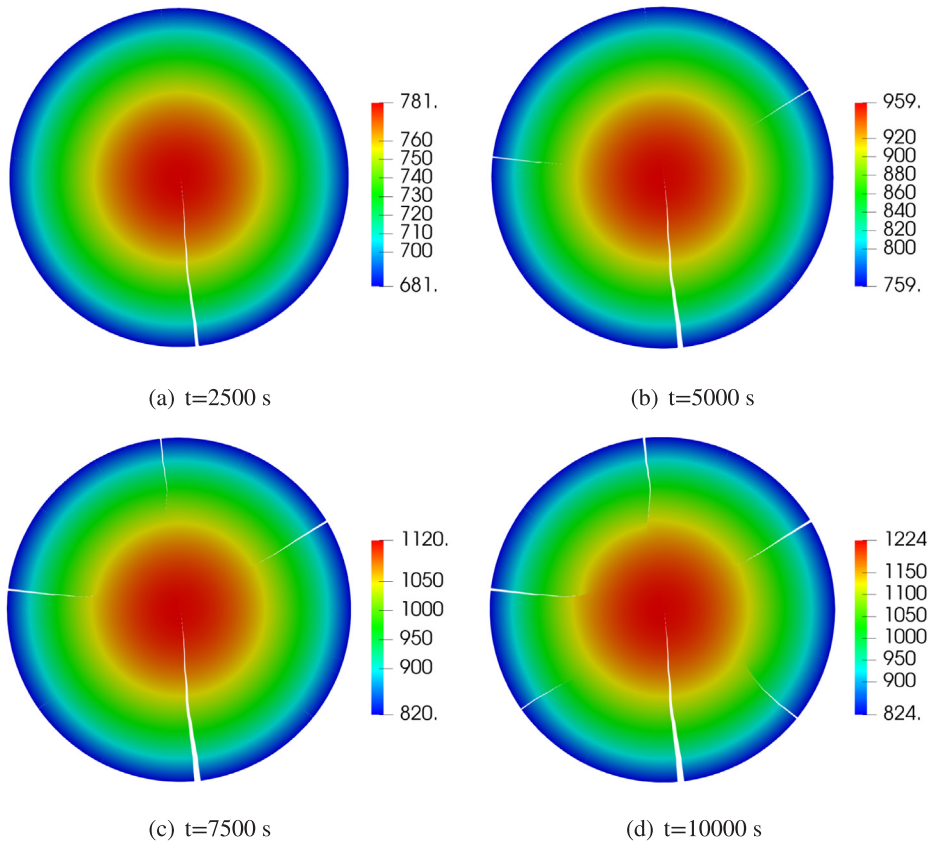


Fig. 19. X-FEM simulation results with critical stress intensity factor of $4 \text{ MPa} \sqrt{m}$ at selected times during power ramp showing displacements (magnified $5\times$) and temperature contours (K).

this study.

The cracks are free to propagate in any direction as dictated by the maximum hoop stress criterion, but they tend to propagate primarily radially inward in all cases studied here. There is no heat transfer across cracks in the model presented here for simplicity. Because the thermal gradient is in the radial direction, there are not significant jumps in the temperature across the cracks when they are in the purely radial direction. However, it can be seen that in areas where the cracks deviate from the radial direction, there are sharp discontinuities in the temperature field. A gap heat transfer model can be included in the X-FEM, and should be considered in future work, as this effect can be important when the gap opening is small, and when thermal gradients normal to cracks are significant, as is the case for cracks oriented in the circumferential direction.

7. Conclusion

This paper provides a summary of the implementation of a phantom node based X-FEM in a multiphysics finite element framework and its application to thermo-mechanical fracture problems. The motivation for this work is to develop a usable engineering capability for modeling fracture propagation in ceramic nuclear fuel. Thermo-mechanical benchmark problems were used to demonstrate the viability of this modeling technique and code implementation, and it was shown to demonstrate very reasonable results for both prescribed stationary cracks and propagating cracks in nuclear fuel.

The X-FEM is well suited for this problem for several reasons. Because it is based on the finite element method, it integrates well with existing finite element-based nuclear fuel performance codes such as Bison. The X-FEM is very effective at representing the effects of discrete cracks, and can use fracture mechanics principles to define their propagation. The phantom-node-based implementation shown here can readily represent discontinuities in all solution fields in a multiphysics analysis. Because the X-FEM only adds additional degrees of freedom for elements that are cut, it does not introduce a significant additional computational overhead relative to the standard FEM.

As shown in this study, the X-FEM is applicable to problems with a single fracture or multiple fractures. Applications of the X-FEM for LWR fuel pellet fracture have demonstrated its applicability for both stationary and propagating cracks. Although it has not been shown in this application, the phantom node approach enables the handling of crack branching and coalescence, which allow it to be used to represent fragmentation. Although the LWR fuel fracture simulation results shown here are generally consistent with other simulation results, there is clearly a need for separate-effects experimental results that can be used to validate models of LWR fuel

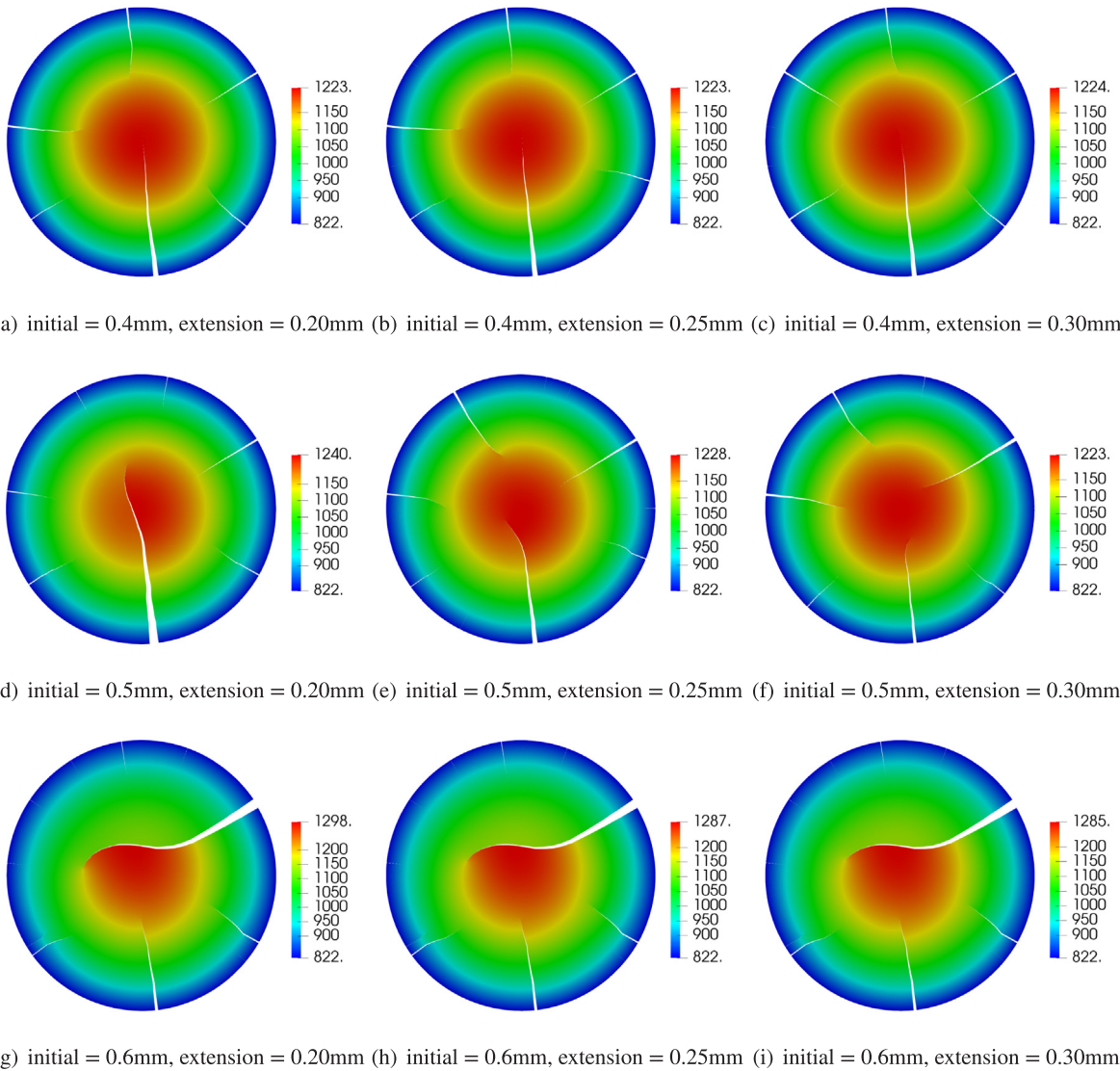


Fig. 20. Sensitivity study of initial crack length and crack extension length (displacements are magnified $5\times$).

fracture.

Perhaps the biggest drawback to the X-FEM is that the method by itself only defines the behavior of the model in the presence of discontinuities, which need to be defined by some means external to X-FEM. For 3-dimensional problems with dynamic crack growth and extensive fragmentation, defining initiation and propagation can be quite challenging. The capability described here is under continuing development, and with further development will begin to address those issues.

Declaration of Competing Interest

There are no conflict of interest in this work.

Acknowledgments

Work supported through the INL Laboratory Directed Research & Development (LDRD) Program under DOE Idaho Operation Office Contract DE-AC07-05ID14517. Work also supported by the Consortium for Advanced Simulation of Light Water Reactors (CASL), an Energy Innovation Hub under the U.S. Department of Energy. This manuscript has been authored by Battelle Energy Alliance, LLC under Contract No. DE-AC07-05ID14517 with the U.S. Department of Energy. The United States Government retains and the publisher, by accepting the article for publication, acknowledges that the United States Government retains a nonexclusive, paid-up, irrevocable, world-wide license to publish or reproduce the published form of this manuscript, or allow others to do so, for

United States Government purposes.

Appendix A. Supplementary material

Supplementary data associated with this article can be found, in the online version, at <https://doi.org/10.1016/j.engfracmech.2019.106713>.

References

- [1] Rashid Y. Mathematical modeling and analysis of fuel rods. *Nucl Eng Des* 1974;29(1):22–32.
- [2] Rashid Y, Dunham R, Montgomery R. Fuel analysis and licensing code: FALCON MOD01. Tech rep EPRI 1011308, Electric Power Research Institute; December 2004.
- [3] Michel B, Sercombe J, Thouvenin G, Chatelet R. 3D fuel cracking modelling in pellet cladding mechanical interaction. *Eng Fract Mech* 2008;75(11):3581–98. <https://doi.org/10.1016/j.engfracmech.2006.12.014>.
- [4] Williamson R, Hales J, Novascone S, Tonks M, Gaston D, Permann C, et al. Multidimensional multiphysics simulation of nuclear fuel behavior. *J Nucl Mater* 2012;423(1–3):149–63. <https://doi.org/10.1016/j.jnucmat.2012.01.012>.
- [5] Rots JG, Blaauwendraad J. Crack models for concrete: discrete or smeared? fixed, multi-directional or rotating?, *HERON*, vol. 34, 1.
- [6] Williamson RL, Knoll DA. Simulating dynamic fracture in oxide fuel pellets using cohesive zone models. In: *Proc SMIRT 20-Division III* (2009) Paper 1775.
- [7] Huang H, Spencer B, Hales J. Discrete element method for simulation of early-life thermal fracturing behavior in ceramic nuclear fuel pellets. *Nucl Eng Des* 2014;278:515–28. <https://doi.org/10.1016/j.nucengdes.2014.05.049>.
- [8] Mella R, Wenman M. Modelling explicit fracture of nuclear fuel pellets using peridynamics. *J Nucl Mater* 2015;467(Part 1):58–67. <https://doi.org/10.1016/j.jnucmat.2015.08.037>.
- [9] Oterkus S, Madenci E. Peridynamic modeling of fuel pellet cracking. *Eng Fract Mech* 2017;176:23–37. <https://doi.org/10.1016/j.engfracmech.2017.02.014>.
- [10] Hu Y, Chen H, Spencer BW, Madenci E. Thermomechanical peridynamic analysis with irregular non-uniform domain discretization. *Eng Fract Mech* 2018;197:92–113. <https://doi.org/10.1016/j.engfracmech.2018.02.006>.
- [11] Wang Y, Zhou X, Kou M. Peridynamic investigation on thermal fracturing behavior of ceramic nuclear fuel pellets under power cycles. *Ceram Int* 2018;44(10):11512–42. <https://doi.org/10.1016/j.ceramint.2018.03.214>.
- [12] Moës N, Dolbow J, Belytschko T. A finite element method for crack growth without remeshing. *Int J Numer Meth Eng* 1999;46(1):131–50. [https://doi.org/10.1002/\(SICI\)1097-0207\(19990910\)46:1<131::AID-NME726>3.0.CO;2-J](https://doi.org/10.1002/(SICI)1097-0207(19990910)46:1<131::AID-NME726>3.0.CO;2-J).
- [13] Spencer B, Huang H, Dolbow J, Hales J. Discrete modeling of early-life thermal fracture in ceramic nuclear fuel. In: *Proceedings of WRFPM 2014*, Paper No. 100061, Sendai, Japan; 2014.
- [14] Belytschko T, Black T. Elastic crack growth in finite elements with minimal remeshing. *Int J Numer Meth Eng* 1999;45(5):601–20. [https://doi.org/10.1002/\(SICI\)1097-0207\(19990620\)45:5<601::AID-NME598>3.0.CO;2-S](https://doi.org/10.1002/(SICI)1097-0207(19990620)45:5<601::AID-NME598>3.0.CO;2-S).
- [15] Hansbo A, Hansbo P. A finite element method for the simulation of strong and weak discontinuities in solid mechanics. *Comput Methods Appl Mech Eng* 2004;193(33):3523–40. <https://doi.org/10.1016/j.cma.2003.12.041>.
- [16] Areias P, Belytschko T. A comment on the article “A finite element method for simulation of strong and weak discontinuities in solid mechanics” by A. Hansbo and P. Hansbo. *Comput. Methods Appl. Mech. Engrg.* 193 (2004) 3523–3540. *Comput Methods Appl Mech Eng* 2006;195(9–12):1275–6. <https://doi.org/10.1016/j.cma.2005.03.006>.
- [17] Song JH, Belytschko T. Dynamic fracture of shells subjected to impulsive loads. *J Appl Mech*, vol. 76, 5, 051301. <https://doi.org/10.1115/1.3129711>.
- [18] Richardson CL, Hegemann J, Sifakis E, Hellrung J, Teran JM. An XFEM method for modeling geometrically elaborate crack propagation in brittle materials. *Int J Numer Meth Eng* 2011;88(10):1042–65. <https://doi.org/10.1002/nme.3211>.
- [19] Song J-H, Areias PMA, Belytschko T. A method for dynamic crack and shear band propagation with phantom nodes. *Int J Numer Meth Eng* 2006;67(6):868–93. <https://doi.org/10.1002/nme.1652>.
- [20] Zhang Z. Finite element methods for interface problems with mesh adaptivity Ph.D. thesis Duke University; 2015.
- [21] Duan Q, Song J-H, Menouillard T, Belytschko T. Element-local level set method for three-dimensional dynamic crack growth. *Int J Numer Meth Eng* 2009;80(12):1520–43.
- [22] Zhang Z, Jiang W, Dolbow JE, Spencer BW. A modified moment-fitted integration scheme for X-FEM applications with history-dependent material data. *Comput Mech* 2018;62(2):233–52. <https://doi.org/10.1007/s00466-018-1544-2>.
- [23] Gaston D, Newman C, Hansen G, Lebrun-Grandié D. MOOSE: a parallel computational framework for coupled systems of nonlinear equations. *Nucl Eng Des* 2009;239(10):1768–78. <https://doi.org/10.1016/j.nucengdes.2009.05.021>.
- [24] Ayachit U. The ParaView guide: a parallel visualization application. *Kitware*; 2015.
- [25] Walters MC, Paulino GH, Dodds RH. Interaction integral procedures for 3-D curved cracks including surface tractions. *Eng Fract Mech* 2005;72(11):1635–63. <https://doi.org/10.1016/j.engfracmech.2005.01.002>.
- [26] Iarve EV, Gurvich MR, Mollenhauer DH, Rose CA, Dávila CG. Mesh-independent matrix cracking and delamination modeling in laminated composites. *Int J Numer Meth Eng* 2011;88(8):749–73. <https://doi.org/10.1002/nme.3195>.
- [27] Strack O, Leavy R, Brannon R. Aleatory uncertainty and scale effects in computational damage models for failure and fragmentation. *Int J Numer Meth Eng* 2015;102(3–4):468–95. <https://doi.org/10.1002/nme.4699>.
- [28] Grogan D, Brádaigh CO, Leen S. A combined XFEM and cohesive zone model for composite laminate microcracking and permeability. *Compos Struct* 2015;120:246–61. <https://doi.org/10.1016/j.compstruct.2014.09.068>.
- [29] Duflo M. The extended finite element method in thermoelastic fracture mechanics. *Int J Numer Meth Eng* 2008;74(5):827–47. <https://doi.org/10.1002/nme.2197>.
- [30] Prasad NNV, Aliabadi MH, Rooke DP. The dual boundary element method for thermoelastic crack problems. *Int J Fract* 1994;66(3):255–72. <https://doi.org/10.1007/BF00042588>.
- [31] Y M. Stress intensity factors handbook. Oxford: Pergamon Press; 1987.
- [32] Prasad NNV, Aliabadi MH, Rooke DP. Incremental crack growth in thermoelastic problems. *Int J Fract* 1994;66(3):R45–50. <https://doi.org/10.1007/BF00042591>.
- [33] Oguma M. Microstructure effects on fracture strength of UO₂ fuel pellets. *J Nucl Sci Technol* 1982;19(12):1005–14.
- [34] Radford K. Effect of fabrication parameters and microstructure on the mechanical strength of UO₂ fuel pellets. *J Nucl Mater* 1979;84(1–2):222–36.
- [35] Kutty TRG, Chandrasekharan KN, Panakkal JP, Ghosh JK. Fracture toughness and fracture surface energy of sintered uranium dioxide fuel pellets. *J Mater Sci Lett* 1987;6(3):260–2.
- [36] Gong B, Frazer D, Yao T, Hosemann P, Tonks M, Lian J. Nano- and micro-indentation testing of sintered UO₂ fuel pellets with controlled microstructure and stoichiometry. *J Nucl Mater* 2019;516:169–77.
- [37] Gatt J-M, Sercombe J, Aubrun I, Ménard J-C. Experimental and numerical study of fracture mechanisms in UO₂ nuclear fuel. *Eng Fail Anal* 2015;47:299–311.